ACCSCIENCE PUBLISHING

Tumor Discovery

ORIGINAL RESEARCH ARTICLE

Malignant versus normal breast tissue: Optical differentiation exploiting hyperspectral imaging system

Mohamed Hisham Aref[1]*, Ibrahim H. Aboughaleb[1], Abdallah Abdelkader Hussein[2], Ayman Mohammed Farag[3], Sara Abd El-Ghaffar[4], and Yasser H. El-Sharkawy[5]

[1]Biomedical Engineering Researcher, Egyptian armed forces, Cairo, Egypt

[2]Department of Histopathology, "Kobri El-Koba" Complex Hospital, Egyptian Armed Forces, Cairo, Egypt

[3]Department of Radiology, Military Medical Academy, Cairo, Egypt

[4]Department of Radiology, Maadi Armed Forces Medical Compound, Cairo, Egypt

[5]Department of Optoelectronics, Military Technical College, Cairo, Egypt

Abstract

Breast malignancy is a critical problem that severely affects women's health globally with a high-frequency rate, necessitating fast, effective, and early diagnostic methods. The present study aims to measure the breast tissue's optical properties by capturing the spectral signatures from malignant and normal breast tissue for therapeutic and diagnostic applications. The optical imaging system incorporates a hyperspectral (HS) camera to capture the spectral signatures for both the malignant and normal breast tissues within 400 ~ 1000 nm. The system was subdivided into two exploratory (reflection/transmission) to measure the tissue's diffuse reflectance (R_d) and light transmission (T_r), respectively. The study involved 30 breast tissue (normal/tumor) samples from 30 females in the age range of 46 ~ 72 years, who were optically inspected in the visible and near-infrared (VIS-NIR) spectra. Then, the inverse adding doubling (IAD) method for breast tissue characterization and descriptive analysis (T-test) was exploited to verify the significant difference between the various types of breast tissues and select the optimum wavelength. Finally, comparing the study outcome with the histopathological examination to evaluate the system's effectiveness by calculation (sensitivity, specificity, and accuracy). The average outcome values demonstrated that the optimal spectral bands distinguishing between the normal and the tumor tissues regarding the reflectance approach were 600 ~ 680 nm and 750 ~ 960 nm at the VIS and NIR spectrum, respectively. Then, for the transmission technique, the optimal spectral bands were 560 ~ 590 nm and 760 ~ 810 nm at the VIS and NIR spectra, respectively. Later, the T-test and the IAD verified that the highest R_d values for discrimination were 600 ~ 640 nm and 800 ~ 840 nm at the VIS and NIR spectra, respectively. On the other side, the highest T_r values were 600 ~ 640 nm and 760 ~ 800 nm at the VIS and NIR spectra, respectively. The investigation's average reading accuracy, sensitivity, and specificity were 85%, 81.88%, and 88.8%, respectively. The experimental trials revealed that the system could identify the optimal wavelength for therapeutic and diagnostic applications through the light interaction behavior of the breast tissue's optical properties.

Keywords: Breast cancer detection; Hyperspectral imaging system; Tissue characterization; Breast biopsy; Optical properties; Visible and near-infrared spectroscopy

***Corresponding author:**
Mohamed Hisham Aref
(MH-Aref@ieee.org)

Citation: Aref MH, Aboughaleb IH, Hussein AA, *et al.*, 2023, Malignant versus normal breast tissue: Optical differentiation exploiting hyperspectral imaging system. *Tumor Discov,* 2(1): 258. https://doi.org/10.36922/td.258

Received: November 15, 2022
Accepted: February 21, 2023
Published Online: March 21, 2023

1. Introduction

Breast malignancy (BM) is a threatening disease in women[1,2]. BM has a high occurrence and mortality rates globally[2]. In line with the World Health Organization's recommendation, it is vital to have an effective healthcare system for BM diagnosis and therapy[3]. Of all women's tumors, 16% are diagnosed with breast cancer[4]. It is the primary source of malignancy-based death in Africa, with an elevated rate in low- and middle-income nations[5,6]. Even though the sign of cancer is not selective to females, the incidence rate of breast cancer in women is multiple times higher than that in men[7]. The malignant-based death, in one way, is credited to late diagnosis as the malignancy has grown in size or metastasized. Consequently, early diagnosis is an excellent approach to improving the survival rate, which can go up to 95%[8].

Early detection of BM was the objective of multiple studies involving imaging modalities[9], such as mammograms[10], ultrasound (US)[11], and breast magnetic resonance imaging (BMRI)[12]. On the other hand, it is limited to several components, for example, the contrast noise ratio[13], longitudinal resolution, and signal-to-noise ratio of every machine[14]. Researchers have investigated numerous breast cancer diagnostic techniques, incorporating X-ray mammogram, MRI, US, positron emission tomography scan, computerized tomography (CT), and tissue removal (biopsy), which are detailed in Table S1 (Supplementary File), for the regular breast cancer diagnostic approaches and their constraints[15].

At present, tissue sampling is the standard method for BM identification. However, it requires acquiring a tumor biopsy and then an investigation by a pathologist[16]. In addition, tissue sampling involves staining, sample cutting, and microscopic investigations, which are time-consuming and costly[17].

None of the abovementioned imaging modalities is flawless for intraoperative resection of malignant tumors[18]. For example, 37% of the women had breast apportioning, and the tumor was allocated at the edge of the biopsy[19]. In oncology, failure to completely eradicate malignant develops cancer recurrence which leads to the spread of the disease[20]. Presently, a pathologist, who investigates the tissue with a digital microscope, surveys the resection edge a couple of days after an operation and following this, the pathologist can give a direct examination before commencing the treatment[21].

The US Food and Drug Administration approved the whole slide imaging (WSI) for the fundamental analysis of histopathological slides[22,23]. Computerized radiology enables immediate investigation of WSI in routine pathology practice. However, there are critical contrasts in motivations for appropriating computerized innovation in pathology when contrasted with radiology. In digital radiology, sensors can straightforwardly catch the data from imaging sources. This advanced cycle obviates the need for ordinary films, harmful compound preparation, and X-ray record rooms. By contrast, slide imaging for pathology necessitates that the tissues are prepared in the typical way (embedded in paraffin, cut, set on glass slides, and stained). Afterward, the pathologist investigates the samples visually thru the microscope, which often consumes time and effort and relies on clinician experience[24].

Several studies compared the frozen section analysis and the imprint cytology involving hematoxylin and eosin (H&E) staining examination alone. *Motomura et al.* reported that compared to H&E, imprint cytology analysis has an overall accuracy, sensitivity, and the specificity of 96%, 90.9%, and 98.5%, respectively[25]. Flett *et al.* stated that frozen section analysis accurately predicts axillary node status with 95%[26]. Moreover, Van Diest *et al.* stated that frozen section examinations were better than imprint cytology analysis (sensitivity 91% versus 63%), and specificity for both methods was 100%[27].

Hyperspectral imaging (HSI) is also called imaging spectrometry and chemical imaging[28]. HSI has advantages over multispectral and RGB imaging because it captures tens to hundreds (continuous spectrum) along the electromagnetic spectrum. HSI collects spatial information (x, y), and a spectral wavelength called a data cube, with each pixel, provides a specific spectral signature based on the reflection, transmission, and absorption of electromagnetic radiation for each material under examination[29]. HSI coordinates ordinary imaging and spectroscopy modalities to provide spatial and spectral information about the object of interest[30,31]. Spectrometry imaging had been exploited in land scanning remotely since 1985[32].

As an imaging methodology for clinical applications, HSI offers extraordinary potential for noninvasive diagnostic and surgical navigation[33]. Several studies highlight the novelty of the HSI in medical applications, *For example,* Fabelo *et al.* used an intraoperative imaging system utilizing HSI to assist in brain tumor delineation to differentiate between normal and cancer tissue in the brain during a neurosurgical operation[34]. In addition, Goto *et al.* implemented a study to recognize gastric tumors in *ex vivo* human tissues[35]. Furthermore, *Regeling et al.* utilized flexible endoscopy combined with an HSI system to discriminate laryngeal cancer to acquire HS cubes in the region within 390 ~ 680 nm[36]. Moreover, HSI had been exploited in monitoring the thermal ablation in the

biological tissue[37,38], sketching of the blood vessels in the arm to aid with Phlebotomy and tissue oxygen[39,40], and breast cancer investigation and malignancy detection[41-43].

The expansion of optical systems in current medical sectors in therapeutic, diagnosis, and surgery regions has motivated the research on optical properties of numerous biological tissues. At the same time, the effectiveness of laser therapy varies by photon propagation and spreading fluence rate inside irradiated tissues[44]. Moreover, the ability to image a biological sample deeply is limited by light penetration depth inside the biological tissues, as distinguished by high turbidity[45]. Regarding the optical properties of the biological tissues (comprising blood, lymph, and other biological fluids), it had been classified into two classes: (i) opaque tissues (intensely scattering) such as the brain, skin, blood, and vascular walls; and (ii) translucent tissues (inadequately scattering) such as the cornea and anterior eye chamber lens[46]. The light interaction (reflection, scattering, and absorption) with the investigated biological soft tissue varies concerning the optical properties variation of its fundamental characteristics, is presented in Figure S1 (Supplementary File).

In this study, we designed an optical imaging system incorporating the hyperspectral (HS) camera to acquire a fast and effective method for breast tissue characterization by capturing the spectral signatures of the malignant and normal breast tissues for both investigative and therapeutic objectives. The exploited optical imaging had been divided into two separate setups (Reflection/Transmission) with spectral range of 380 – 1050 nm to measure the tissue's diffuse reflectance (R_d) and light transmission (T_r), and then the sample absorption coefficient (μ_a) was calculated from T_r. Then, from the measurements of the previously stated parameters for both the normal and the malignant breast tissues, we exploited the inverse adding doubling (IAD) method for breast tissue characterization. Furthermore, the T-test was utilized to verify the significant difference between the various types of breast tissues and select the optimum wavelength for diagnosis and therapy applications. Finally, the proposed methods with histopathological examination were compared to evaluate the system's effectiveness in terms of sensitivity, specificity, and accuracy.

2. Materials and methods

2.1. Primary system interconnections

The primary system interconnections include the following:

- The design and implementation of the optical imaging system
- The optical phantoms and system calibration
- The investigation and patient criteria for breast tissue samples selection and preparation
- Capturing the HS image for the *ex vivo* breast samples
- The measurement of the sample's diffuse reflection (R_d) for both the cancerous and the non-cancerous regions
- The measurements for sample T_r
- Calculating the sample absorption coefficient (μ_a) from the measured T_r
- The statistical analysis to select the optimum wavelength for the diagnostic and therapeutic applications
- Calculating the system efficiency (average reading accuracy, sensitivity, and specificity).

2.2. Design and implementation of the optical imaging system

The principal structure of the proposed framework is partitioned into two different configurations. The first configuration (reflection approach) utilizes a polychromatic source light (Derungs, 20P SX -20 Watt, Germany) with a spectral range (400 ~ 950 nm) to measure the R_d of the investigated *ex vivo* breast samples, as illustrated in Figure 1A for the schematic diagram and Figure 1B for the actual setup[47]. The second configuration (transmission approach) employs the same light source. However, underneath the investigated samples for light T_r measurement, these measurements yield the calculation of the μ_a, as presented in Figure 1C for the schematic diagram and Figure 1D for the actual setup.

Both configurations exploit the HS camera (Surface Optics, SOC710, USA) at 400 ~ 1000 nm, with a spectral resolution of 4.69 nm and a bit depth of 12, which is equipped with an objective lens (Schneider, 400 – 1000 nm, Germany). The employed HS camera is a push broom imager with scanned cube 128 frames which has a built-in translation sensor capable of directly collecting information for the entire spatial image of the whole object. The camera was settled at a height of 20 cm, and the light source was 16 cm from the breast samples. The light was settled at the same distance under the samples in the transmission configuration. The signal analysis measurements were analyzed with software (SOC's Hyperscanner and SRAnalysis, USA) accompanied by (DADiSP, SE 6.7, USA) on a personal laptop (DELL, INSPIRON 5584, Intel Core I7, 16 GB RAM, Windows 10, USA) where the actual setup with all of its components is displayed in Figure 1.

2.3. Optical phantom preparation and system calibration

Initially, we prepared liquid optical phantoms for system calibration. Then, we used demineralized water as a matrix material and added milk (whole milk, lactose-free, and fat-free) as the scattering material with three different

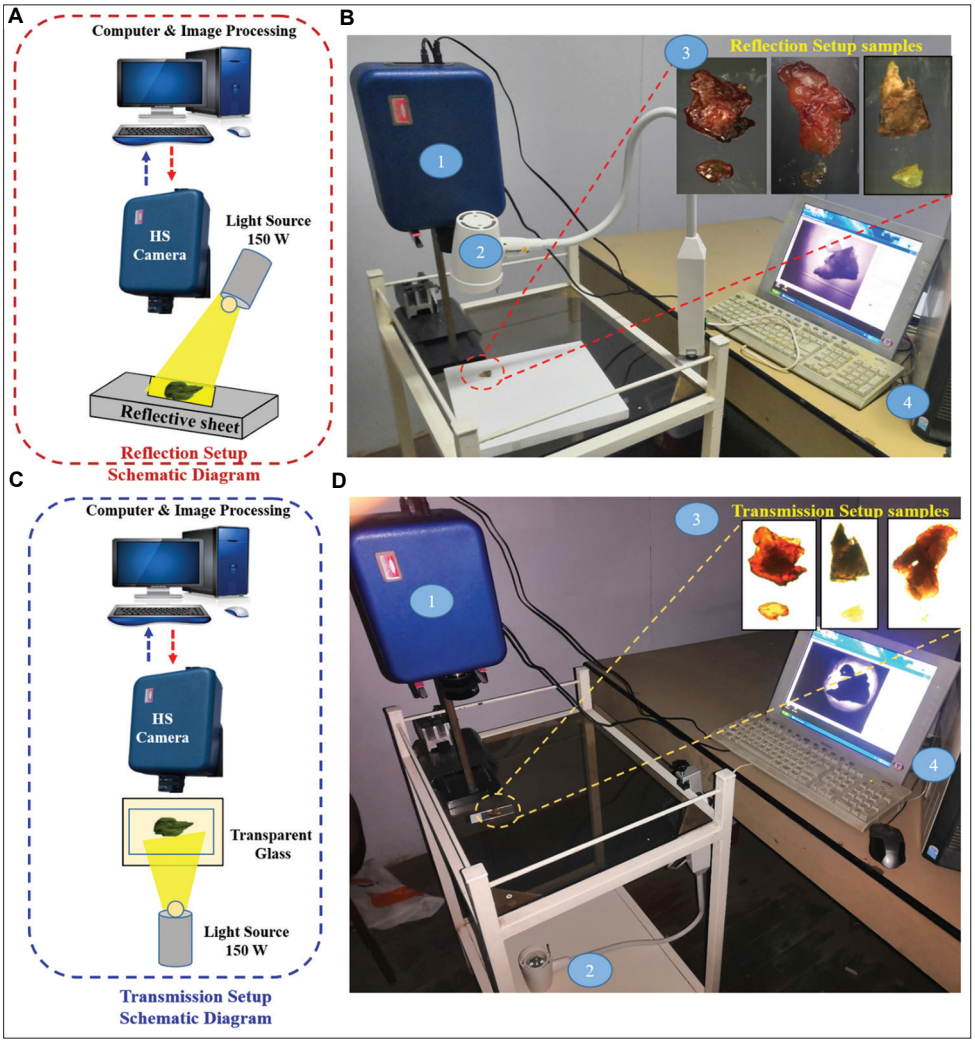

Figure 1. (A) The schematic diagram of the reflection setup. (B) The actual reflection setup to measure the tissue's diffuse reflectance (R_d): (1) the HS camera, (2) the polychromatic source light, (3) the investigated breast samples, and (4) the computer and the image software analysis. (C) The schematic diagram of the transmission setup. (D) The actual transmission setup to measure the tissue's light transmission (T_t).

fat concentrations (3%, 1.75%, and 0%). Samples were arranged in a 300 mL beaker, mixing the milk with the water to achieve various lipid concentrations (0.1% ~ 1%, with increments of 0.05%). Moreover, the exploited absorption material was a red Indian ink (Speedball, Statesville, USA) with whole fat milk (3% of fat concentration). Mixture was prepared by adding 200 mL from the ink with 0.2 mL of milk at concentration range (0.005% ~ 0.2%). The ink concentration was constant at 0.1% with 200 µL dilution in 100 mL of demineralized water. Milk was added to the mixture with a syringe of 5 mL of lipid at various concentrations (0.1% ~ 0.5%)[48,49].

2.4. Patient criteria and sample preparation

The current trial examination was approved by the Institutional Ethical Committee. In addition, all patients read and signed the consent form before data collection began. The study was conducted from May 2020 to October 2021 with a total of 30 female patients who were diagnosed with breast cancer by two different imaging methods (mammogram/US) and had underwent mastectomy; the patient data for the present study are summarized in Table S2 (Supplementary File).

The breast tumor samples, which had been classified by the pathologists, were processed at the pathological center and then attached with the complete histology lab report for each patient. The breast samples were cut by the pathologist into various sizes around 10 ~ 12 cm^2 with a thickness of 4 ~ 5 mm. One of the team members transported samples in an icebox. During the experimental investigation, samples were dipped in phosphate-buffered saline (pH = 7.4) to remove blood. After scanning, the

samples were stored in a freezer at a temperature of −75°C. The experimental trials were conducted in a lab with room temperature of ~25°C.

2.5. Principal theory and procedure equations

The proliferation of incident light inside tissue is a significant issue in clinical applications and the improvement of diagnostic techniques. This way, this segment is committed to a concise audit of the light tissue collaboration systems, optical cycles included in HSI, and valuable diagnostic and therapeutic data provided by HSI[33]. Light entering biological breast tissue goes through multiple scattering and absorption as it proliferates across the tissue[50]. Biological tissues are assorted in composition through spectral distinctions in optical properties. Scattering appears where there is a spectral distinction in the refractive index[51].

The diffusion profundity of light into biological tissues depends on how unequivocally the tissue absorbs light. Most tissues are adequately powerless absorbers to allow substantial light diffusion inside the therapeutic window, going from 600 to 1300 nm. Inside the therapeutic window, scattering is higher than absorption, so the spreading light gets diffuse[50,51]. The primary block diagram of the two applied system approaches (reflection and transmission) is illustrated in Figure 2.

Light proliferation in investigated tissue depends on the transport hypothesis[52,53]. Transport theory depends on the superposition of energy flux, so the wave properties of light (polarization and interference) are not considered in transport theory. Where the radiant power of the light transferred to the surface is displayed in Equation I:

$$\text{Ṛ}= \int \text{Ḟ}.\text{n}\, dA \tag{I}$$

Where (Ḟ) is the flux vector, (Ṛ) is the radiant power transferred through a surface with the area (A).

As the surface of the biological tissue is not homogeneous leading to light proliferation. However, it is crucial to understand a few of the significant optical parameters which are exploited in modeling of the light proliferation, such as the propagation of photons, fluence ratio, radiance, and flux[54].

The photon allocation function $\text{Ṇ}(\dot{\text{r}},\hat{\text{ṣ}})$ is defined as the number of photons for each unit volume moving in the course of a unit vector $\hat{\text{V}}$, in the component of fixed angle incorporating $\hat{\text{V}}$ at a specified spot ṛ divided by this component. The power of photons (β) that proliferate through minute area $d\breve{\text{A}}$ in the minute fixed angle (dw) in the course of $\hat{\text{V}}$, with energy hν and speed $\acute{\text{S}}_t$ is shown in Equation II:

$$d\beta(\dot{\text{r}},\hat{\text{ṣ}})[W] = \text{Ṇ}(\dot{\text{r}},\hat{\text{ṣ}})\, d\text{Ạ}\, dw\, \acute{\text{S}}_t\, \text{hν} \tag{II}$$

Where $(\acute{\text{S}}_t)$ is the speed of light in tissue and $(d\breve{\text{A}})$ is perpendicular to $\hat{\text{V}}$.

Very often, the operating mechanism of medical techniques exploits the relations of light spreading through tissue. The quantity of light could be stated as the irradiance $\breve{\text{Ḛ}}_0$, which is the radiant energy flux of the surface element divided by surface area. Part of the incident light is reflected, and the others are attenuated with the tissue by diffuse reflection and absorption according to the Beer's law, as shown in Equations III and IV.

$$\omega(\hat{\text{Ḷ}}) = \breve{\text{Ḛ}}_0\,(1-\text{Ṛ})(e^{(-(\mu_a-\mu_s)\dot{\text{Ḷ}})}) \tag{III}$$

Where ω $(\hat{\text{Ḷ}})$ is the fluence ratio for the unscattered beam at location $(\hat{\text{Ḷ}})$ $\breve{\text{Ḛ}}_0$ is the irradiance, and Ṛ is the surface reflection (Fresnel).

$$\psi = \frac{1}{(\breve{\text{R}}\text{d}+\mu_a)} = \frac{1}{\mu_t} \tag{IV}$$

Where R_d is the scattering (diffuse reflection) coefficient, μ_a is the absorption coefficient, μ_t is the total attenuation coefficient, and ψ is the penetration depth.

While light travels within the tissue, its intensity gradually weakens, in a phenomenon known as light absorption and expressed by μ_a, which is described as the probability of photon absorption after being proliferated per unit length. The light absorption follows the Lambert-Beer law. Therefore, when there are only light absorption phenomena of tissue, it could be expressed by Equation V. Additionally, the optical homogenous scattering phenomena follows Lambert-Beer law and could also be expressed by Equation VI[55].

$$I = I_{0\,e^{-\mu_a d}} \tag{V}$$

$$I = I_{0\,e^{-\mu_s d}} \tag{VI}$$

Where μ_a is known as the absorption coefficient, I_0 is the incident light, I is the light intensity after passage through the medium or tissue, and (μ_s) is the scattering coefficient.

The incident light beam interaction with the biological tissues is evaluated in terms of T_r, R_d, and calculated absorption coefficient (μ_a)[54], using Equations VII and VIII:

$$\text{Tr} = \frac{\text{Ṭ}_{\breve{\text{R}}\text{d}}-\text{Ṭ}_0}{\text{Ṭ}_{\breve{\text{R}}\text{d}t}-\text{Ṭ}_0} \tag{VII}$$

$$\mu_a = \frac{\mu_{a_{\breve{\text{R}}\text{d}}}-\mu_{a_0}}{\mu_{a_{\breve{\text{R}}\text{d}t}}-\mu_{a_0}} \tag{VIII}$$

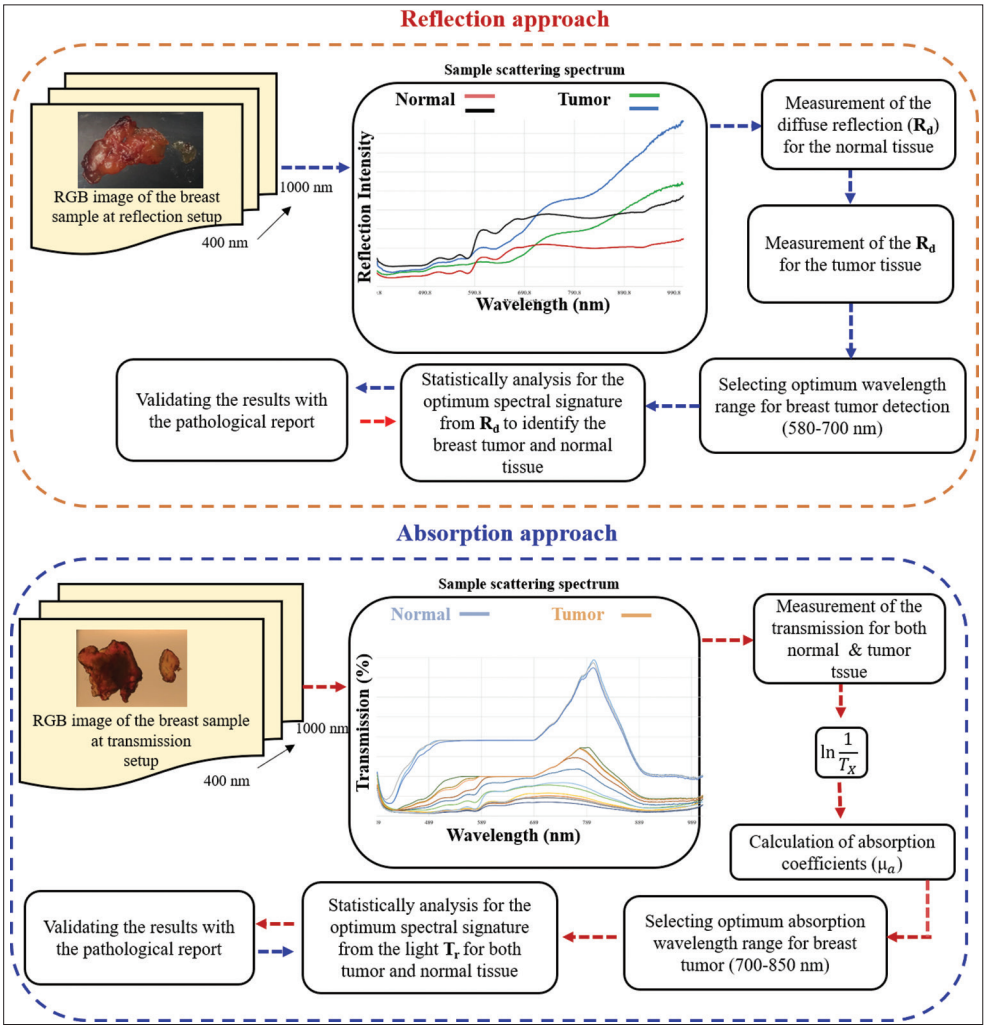

Figure 2. The main block diagram of the two applied system approaches (reflection/transmission) to measure the tissue's diffuse reflectance (R_d) and light transmission (T_r), which highlight the signal analysis for the optical properties and capture the spectral signatures of the investigated *ex vivo* breast tissue samples.

Where $\frac{\mu a_{\tilde{R}d}}{T_S}$ and $\frac{\mu a_{\tilde{R}dt}}{T_{St}}$ are the measured light intensity by R_d/T_r with the investigated breast tissue and the typical white plate reflection, respectively. The $\frac{\mu a_0}{T_0}$ demonstrates the background light intensity discriminated by R_d/T_r without the sample reflection on the plate.

2.6. Spectral arrangement

The hyper spectral images were taken for every investigated breast tissue sample from the two different arrangements as explained previously with spatial pixels (max/nominal) = 1040/520, spectral channels = 128, HS cube captured 100 frames/s within 6.96 s/cube. They applied statistical analysis for the spectral signature for selecting the optimum spectral range to discriminate the normal from the abnormal tissue.

It is essential to capture two data cubes each time a breast sample is imaged: the first one is the dark data cube which represents the image sensor's dark current, and the second one is for a standard white reference for spectral calibration[56]. First, the acquired dark cube was taken by closing the lens of the HS camera with its cap. The data of the dark and white cubes were exploited to adjust the reflected sample image to remove the noise impacts of the investigated sample tissue, as expressed in Equation IX:

$$\ddot{R}_f(\vartheta) = \frac{\tilde{I}_m(\vartheta) - \tilde{I}_d(\vartheta)}{\tilde{I}_w(\vartheta) - \tilde{I}_d(\vartheta)} \times 100\% \quad \text{(IX)}$$

Where $\ddot{R}_f(\vartheta)$ is the relative reflectance of the investigated sample image, $\tilde{I}_m(\vartheta)$ is the seized image, $\tilde{I}_d(\vartheta)$ is the opaque image cube, and $\tilde{I}_w(\vartheta)$ is the attained image of the white reflectance board.

2.7. Statistical analysis

So far, the commonly used methods to calculate the scattering and absorption properties of the various mediums are:

(i) Monte Carlo (MC), which is a general class of computational algorithms to achieve a numerical outcome by relying on random sampling. MC in the optical field is effective for a broad range of light μa, μs, and photon paths[57].
(ii) Diffuse approximation (DA), which is an alternative calculation method to calculate the scattering and absorption properties of turbid mediums[58].
(iii) IAD, which is an extended method from the adding double (AD) method, and exploited to solve the radiative transport equation in the optical field sector related to the light's interaction with the tissues in a slab geometry[59].

The radiative transport equation could be used to achieve light intensity distribution for the physical mediums, as shown in Equation X[60].

$$\frac{dI(r,s)}{ds} = -(\mu_a + \mu_s) I(r,s) + \frac{\mu_s}{4\pi} \int_{4\pi} p(s,s') I(r,s') d\theta \quad (X)$$

Where $I(r,s)$ is the measured intensity per unit length, r is the target location, s is the unit direction vector, $p(s,s')$ is the phase function, and θ is the solid angle.

Although there is no analytical solution for Equation X, it is achievable by exploiting the MC technique[61,62]. Moreover, the IAD method is used to solve the radiative transport equation. IAD technique and MC model have offered more precise approximations of optical properties for the biological tissue (μ_a, μ_s, g) better than other methods. Two dimensionless quantities are exploited in the whole process of the IAD, that is, the albedo (a) and the optical depth ($\mathcal{T}$), which are well-defined in Equations XI and XII:

$$a = \frac{\mu_s}{\mu_s + \mu_a} \quad (XI)$$

$$\mathcal{T} = t(\mu_s + \mu_a) \quad (XII)$$

Where is the sample's thickness (mm), the measured values of R_d, the total diffuse transmittance (T_d), and the unscattered collimated transmittance (T_c) are applied to the IAD process to calculate the (μ_a, μ_s).

Due to the minimum computational time and high accuracy comparable to both DA and MC methods, we exploited in our system the IAD method for breast tissue characterization and descriptive analysis (T-test) to verify the significant differences among the various types of breast tissues and to select the optimum wavelength.

2.8. System efficiency analysis

The efficiency of the presented system analysis methods is achieved by comparing the outcomes with the histological investigations. Regarding the results of these comparisons, three numerical values (sensitivity, specificity, and accuracy) could be measured to evaluate the various spectral analysis methods, as shown in Equations XIII, XIV, and XV:

$$\text{Sensitivity} = \frac{TP}{TP + FN} \quad (XIII)$$

$$\text{Specificity} = \frac{TN}{TN + FP} \quad (XIV)$$

$$\text{Accuracy} = \frac{TP + TN}{\text{Total no. of samples}} = \frac{TP + TN}{TP + TN + FP + FN} \quad (XV)$$

Where true positive (TP) is the cases detected by the proposed system as actual masses (tumors); false negative (FN) is the cases of the system which had not been detected and have masses; true negative (TN) is the cases detected by the proposed system as normal, and they are normal cases; and false positive (FP) is the cases mistakenly detected by the presented system as abnormal masses, and they are normal cases.

3. Results

Our primary goal of these assessments is to investigate the optical properties of the *ex vivo* breast samples (normal/tumor) by identifying the spectral signatures through incorporating the HS camera capabilities to provide the essential data for diagnostic and therapeutic applications concerning breast cancer. We set up two diverse frameworks (reflection/transmission) methods using the HS camera at wavelength range (400 ~ 1000 nm) and with a polychromatic light source in the VIS-NIR range for this examination.

We initially exploited the first framework (reflection method) to measure the investigated *ex vivo* breast tissue sample's light R_d; one of the investigated cases is presented in Figure 3. The solid red line represents the measured tumor tissue's R_d spectrum, and the solid blue line identifies the normal tissue's R_d spectrum over the VIS-NIR range. From the measured light R_d for the investigated samples, we could visually highlight the spectrum peaks, which distinguish between the normal and the tumor tissues at wavelength range 600 ~ 680 nm and 750 ~ 960 nm at the VIS range and NIR range, respectively.

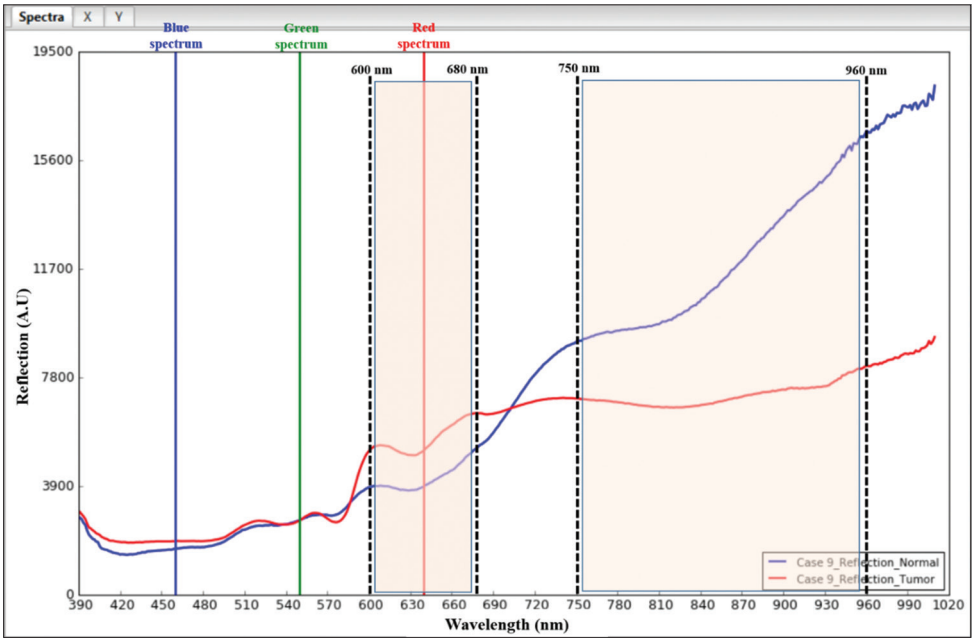

Figure 3. The measured light R_d spectrum for one of the investigated samples (patient ID 1009). The solid red line is for the measured tumor tissue's light R_d spectrum, and the solid blue line identifies the measured normal tissue's R_d spectrum highlighting the peaks which could visually identify between both normal and tumor tissues at wavelength ranges of 600 ~ 680 nm and 750 ~ 960 nm at the visible and near-infrared spectra, respectively.

Moreover, regarding the second framework (transmission method) to measure the investigated *ex vivo* breast tissue sample's light T_r, one of the investigated cases is presented in Figure 4. The solid red line represents the measured tumor tissue's T_r spectrum, and the solid blue line identifies the normal tissue's T_r spectrum over the VIS-NIR range. From the measured light T_r for the investigated samples, we could visually highlight the spectrum peaks that distinguish between the normal and the tumor tissues at wavelength range 560 ~ 590 nm and 760 ~ 810 nm at the VIS range and NIR range, respectively.

From the two frameworks, we could measure the tissue's R_d and light T_r, and then calculate the sample μ_a from the measured T_r. Then, from the measurements of the previously stated parameters for both the normal and the malignant breast tissues, we could identify a spectral signature for each tissue type by investigating the optical spectroscopy in the VIS-NIR range for the measured light R_d and T_r. The measured tissue's R_d, T_r, and calculated μ_a of the investigated *ex vivo* breast samples are illustrated in Figure S2A-C (Supplementary File), respectively.

Later, we exploited the IAD method for breast tissue characterization and the descriptive analysis (T-test) to verify the significant difference between the various types of breast tissues and select the optimum wavelength. From the T-test and the IAD regarding the measured R_d, we could verify that the highest R_d values for discrimination were 600 ~ 640 nm at the VIS range and 800 ~ 840 nm at the NIR range, with the minimum tolerance error, as shown in Figure 5.

On the other side, the highest T_r values were 560 ~ 600 nm at the VIS range. Since the tolerance error was high in tumor measurements, it was better to select the wavelength range of 600 ~ 640 nm at the VIS range. Meanwhile, the wavelength range of 760 ~ 800 nm at the NIR range was with the minimum tolerance error, as shown in Figure 6.

Finally, we compared the system outcome with the pathological reports to evaluate the system efficiency and calculate the three numerical values (sensitivity, specificity, and accuracy). Where, the corrected prediction of the system (TP and TN) is compared with the pathological report for each region (malignant in red color and non-malignant in blue color), as shown in Figure 7A. Figure 7B shows the receiver operating characteristic (ROC) curve data illustrating the normal and tumor data to highlight the effect of the cut-off point on decision-making concerning the designed machine learning model. Figure 7C shows the ROC curve to highlight the test's sensitivity (TP rate) and specificity (FP rate) at various cutoff values.

4. Discussion

BM is the second most common cancer in women after skin cancer globally[63]. BM is a threatening disease in both incidence and mortality rates. Therefore, early

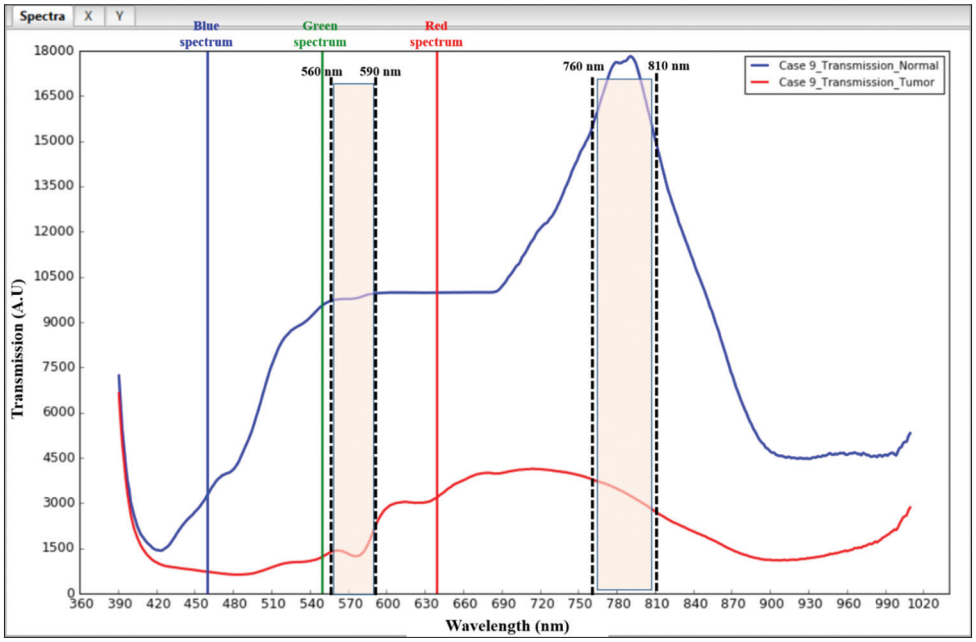

Figure 4. The measured light T_r spectrum for one of the investigated samples (patient ID 1009). The solid red line is for the measured tumor tissue's light T_r spectrum, and the solid blue line identifies the measured normal tissue's T_r spectrum highlighting the peaks which could visually identify between both normal and tumor tissues at wavelength ranges of 560 ~ 590 nm and 760 ~ 810 nm at the visible and near-infrared spectra, respectively.

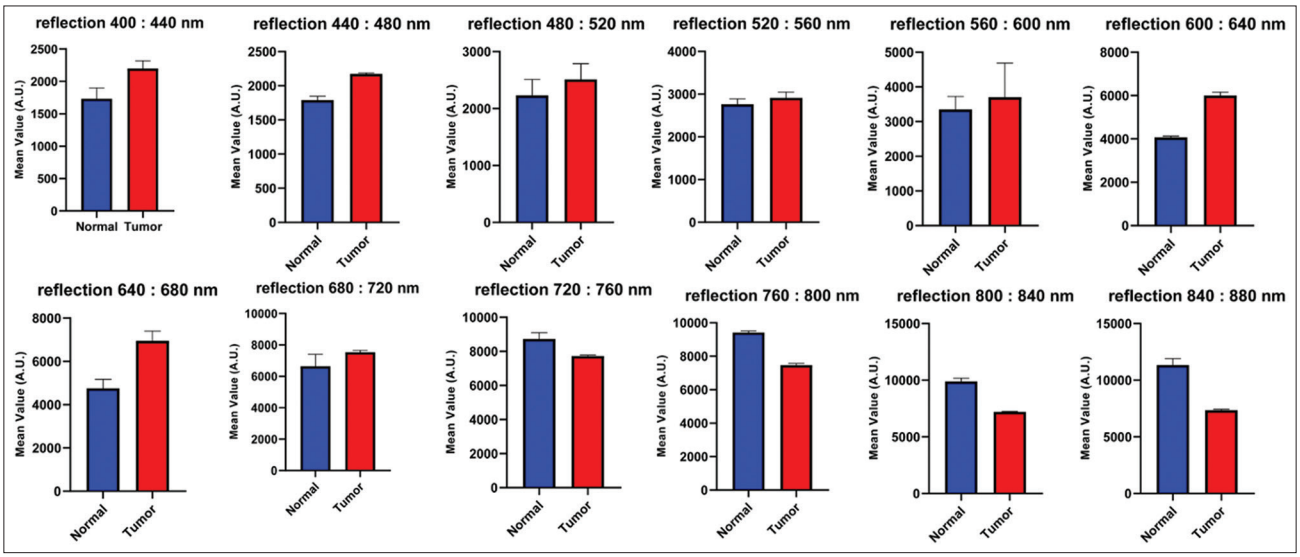

Figure 5. The chart analysis of the inverse adding doubling method associated with the T-test for the measured diffuse reflection (R_d) signatures of the investigated *ex vivo* breast samples from both the normal and breast tumor at the visible and near-infrared (VIS-NIR) spectrum range (400 ~ 1000 nm), with resolution of 40 nm over twelve groups, where the highest R_d values for discrimination were 600 ~ 640 nm at the VIS range and 800 ~ 840 nm at the NIR range, with the minimum tolerance error.

diagnosis is vital for life-saving[64,65], which could go up to 95%[8]. Breast-conserving surgery (BCS) is a common therapy. However, clear surgical margins are vital to avoid cancer recurrence. Additionally, intraoperative pathologic diagnostic techniques, such as imprint cytology and frozen section analysis, are well-known essential tools in BCS. In addition to the traditional methods, there are also modern methods, which have various advantages and disadvantages (Table 1)[66].

Recently, there has been a rapid development in the research of optical methods in the biomedical field sector, leading to a growing number of commercial diagnostic and therapeutic methods. The HSI is a capable non-

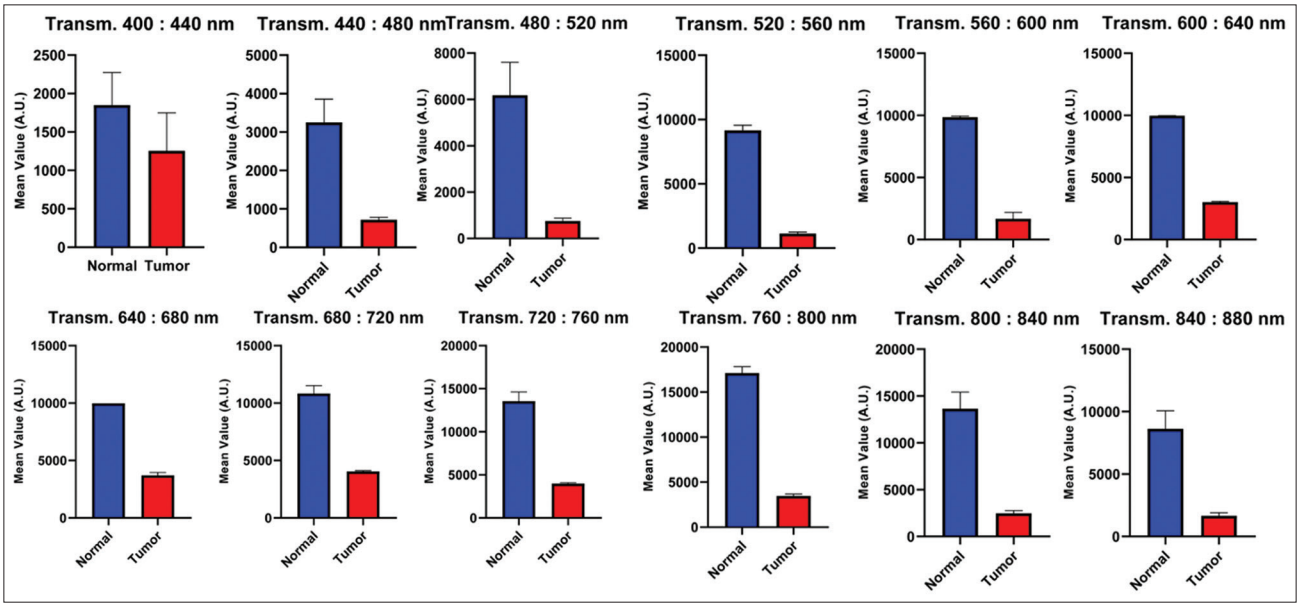

Figure 6. The chart analysis of the inverse adding doubling method associated with the T-test for the measured light transmission (T_r) signatures of the investigated *ex vivo* breast samples from both the normal and breast tumor at the visible and near-infrared (VIS-NIR) spectrum range (400 ~ 1000 nm), with resolution of 40 nm over twelve groups, where the highest T_r values for discrimination were 600 ~ 640 nm at the VIS range and 760 ~ 800 nm at the NIR range, with the minimum tolerance error.

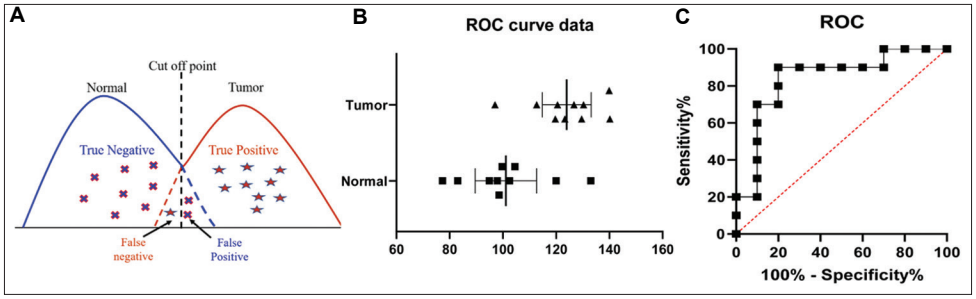

Figure 7. (A) The system outcome where the tumor samples illustrated in red font and normal samples in blue font versus the estimation differences to show the correct prediction and the missed diagnosis in each trial. (B) The receiver operating characteristic (ROC) curve data which represent the normal and tumor data to highlight the effect of the cutoff point on decision-making concerning the designed machine learning model. (C) The ROC curve demonstrating the sensitivity (true positive rate) and specificity (false positive rate) of the test at various cut-off values.

invasive, non-ionizing method that encourages fast achievement and analysis of diagnostic data in the medical field[67]. McCormack *et al.* proposed an optical imaging system incorporating the HS camera, which was capable to map oxygen saturation, vessel density and branching in cancer microvasculature with high resolution to successfully computing malignant microvascular response on anti-cancer therapy over a long period of time[68]. In addition, Kim *et al.* proposed an algorithm to extract the region of interest (ROI) from the HS images of BM samples instead of the visual or manual inspection[69]. Moreover, Pourreza-Shahri *et al.* suggested a classification algorithm to identify the BM margins in the HS images with a sensitivity of 98% and a specificity of 99%[70].

Globally, up to 40% of the BCS necessitate additional surgical procedures due to positive resection margins. Therefore, numerous researchers propose techniques to reduce this value by assessing the resection margins in real time using the HSI system during surgery[71]. The novel techniques in breast cancer investigation exploiting the HSI are briefly depicted in Table S3.

Figure 3 illustrates the first approach of measuring the R_d of the investigated *ex vivo* breast tissue samples. The solid red line represents the measured tumor tissue's R_d spectrum, and the solid blue line represents the normal tissue's R_d spectrum. We noticed from the graph plot that we could visually differentiate between the tumor and the normal tissue at wavelength range of 600 ~ 680 nm and 750

Table 1. Summary of the conventional pathologic methods for the breast-conserving surgery (BCS) and a simple illustration of the proposed new techniques with respect to the gold standard BCS (frozen section analysis).

Technique	Complexity	Process speed	Cost	Margin evaluation	Morphology
Imprint cytology [72]	Simple	Fast	Cost-effective	√	×
Frozen section [66]	Complex	Time-consuming	Expensive	√	√
H&E associated with artificial intelligence [73]	Complex	Fast	Cost-effective	×	√
Standard specimen radiography [74]	Simple	Fast	Cost-effective	√	×
Optical coherence tomography [75]	Simple	Fast	Expensive	×	×
Ultraviolet-photoacoustic microscopy [76]	Simple	Time-consuming	Expensive	×	√
Intraoperative ultrasonography [77]	Simple	Fast	Cost-effective	√	×
Micro-computed tomography [78]	Simple	Fast	Expensive	×	×
Radiofrequency spectroscopy [79]	Simple	Fast	Cost-effective	√	×
Bioimpedance spectroscopy [80]	Simple	Fast	Cost-effective	√	×
HSI attached with standard microscope and deep learning [81]	Complex	Fast	Cost-effective	√	×

~ 960 nm at the VIS and NIR ranges, respectively. Then, from the second framework, we could measure the light T_r, and from the graph, we could visually distinguish between the normal and the tumor tissues at wavelength range of 560 ~ 590 nm and 760 ~ 810 nm in the VIS range and NIR range, respectively.

From the two methods (reflection/transmission), we could calculate the sample μ_a from the measured T_r. Then, we could identify a spectral signature for each tissue type in the VIS-NIR range from the measurements of the previously stated parameters for both the normal and the malignant breast tissues. The measured light tissue's R_d, T_r, and calculated μ_a of the investigated *ex vivo* breast samples are illustrated in Figure S2A-C (Supplementary File), respectively.

Furthermore, we exploited the IAD method for breast tissue characterization and the T-test to verify the significant difference among the various types of breast tissues and to select the optimum wavelength. From the T-test and the IAD regarding the measured R_d, we could verify that the highest R_d values for discrimination were 600 ~ 640 nm at the VIS range and 800 ~ 840 nm at the NIR range, with the minimum tolerance error, as shown in Figure 5**.** On the other side, the highest T_r values were 590 ~ 600 nm at the VIS range. Since the tolerance error was high in tumor measurements, it was better to select the wavelength range of 600 ~ 640 nm at the VIS range. Meanwhile, the wavelength range of 760 ~ 800 nm at the NIR range was with the minimum tolerance error, as shown in Figure 6.

Finally, to evaluate the system efficiency, we compared the system outcome versus the pathological reports to calculate the corrected prediction (TP) and the incorrect prediction (FP), alongside the FN and TN. Regarding these values, we could plot the ROC curve and determine the system performance (accuracy: 85%; sensitivity: 81.88%; and specificity: 88.8%).

5. Conclusions

The current study showed that the potential and capabilities of HS camera in providing a rapid and non-invasive method to measure the breast tissue's optical properties by capturing the spectral signatures from the malignant and normal breast tissue and to distinguish between them in both the diagnostic and therapeutic applications. The light traveling through tissue was exposed according to two parameters, R_d and μ_a, which depend on the optical properties of the breast tissue. Finally, we conclude from the Rd measurements of the investigated breast samples, that wavelength ranges 600 ~ 640 nm and 800 ~ 840 nm are the optimum ranges to identify the cancerous and non- cancerous regions regarding the diagnostic purpose at the VIS, and NIR spectrum. However, from the Tr values (therapeutic applications), the ideal wavelength ranges were 600 ~ 640 nm, and 760 ~ 800 nm. In the present study, the average accuracy, sensitivity, and specificity were 85%, 81.88%, and 88.8%, respectively. In future work, we intend to explore this direction in infrared band using a commercial and low-cost spectral detector to calculate the optimum wavelength with the highest R_d value to develop an alternative low-cost and rapid diagnostic technique of breast cancer.

Acknowledgments

None.

Funding

None.

Conflict of interest

The authors declare no conflict of interest.

Author contributions

Conceptualization: Mohamed Hisham Aref, Ibrahim H. Aboughaleb, Yasser H. El-Sharkawy

Investigation: Mohamed Hisham Aref, Ibrahim H. Aboughaleb

Resources: Abdallah Abdelkader Hussein, Ayman Mohammed Farag, Sara Abd El-Ghaffar

Supervision: Ayman Mohammed Farag, Sara Abd El-Ghaffar, Yasser H. El-Sharkawy

Writing – original draft: Mohamed Hisham Aref, Ibrahim H. Aboughaleb

Writing – review & editing: Yasser H. El-Sharkawy

Ethics approval and consent to participate

No experimental investigation was performed on any individuals within this study and all patients read and signed two copies of a consent form before the beginning of data collection.

Consent for publication

All the authors declare that all the participated patients had been well informed about the investigation. All patients read and signed two copies of a consent form before the beginning of data collection, patient data had been coded and summarized in Table S2 in Supplementary file.

Availability of data

The authors stated and declare that all the datasets used and/or analyzed during the current study are available from the corresponding author on reasonable request.

References

1. Ferlay J, Colombet M, Soerjomataram I, *et al*., 2021, Cancer statistics for the year 2020: An overview. *Int J Cancer*, 149(4): 778–789.

   https://doi.org/10.1002/ijc.33588

2. Sung H, Ferlay J, Siegel RL, *et al*., 2021, Global cancer statistics 2020: GLOBOCAN estimates of incidence and mortality worldwide for 36 cancers in 185 countries. *CA Cancer J Clin*, 71(3): 209–249.

   https://doi.org/10.3322/caac.21660

3. World Health Organization, 2021, World Health Statistics 2021. Geneva: World Health Organization.

4. Fitzmaurice C, Dicker D, Pain A, *et al*., 2015, The global burden of cancer 2013. *JAMA Oncol*, 1(4): 505–527.

   https://doi.org/10.1001/jamaoncol.2015.0735

5. Ferlay J, Soerjomataram I, Dikshit R, *et al*., 2015, Cancer incidence and mortality worldwide: Sources, methods and major patterns in GLOBOCAN 2012. *Int J Cancer*, 136(5): E359–E386.

   https://doi/org/10.1002/ijc.29210

6. Mody GN, Nduaguba A, Ntirenganya F, *et al*., 2013, Characteristics and presentation of patients with breast cancer in Rwanda. *Am J Surg*, 205(4): 409–413.

   https://doi.org/10.1016/j.amjsurg.2013.01.002

7. Faust O, Acharya UR, Meiburger KM, *et al*., 2018, Comparative assessment of texture features for the identification of cancer in ultrasound images: A review. *Biocybern Biomed Eng*, 38(2): 275–296.

8. Etehadtavakol M, Ng EY, 2013, Breast thermography as a potential non-contact method in the early detection of cancer: A review. *J Mech Med Biol*, 13(2): 1330001.

9. Nofiele JT, Czarnota GJ, Cheng HL, 2014, Noninvasive manganese-enhanced magnetic resonance imaging for early detection of breast cancer metastatic potential. *Mol Imaging*, 13(1): 1–10.

   https://doi.org/10.2310/7290.2013.00071

10. Gøtzsche PC, Jørgensen KJ, 2013, Screening for breast cancer with mammography. *Cochrane Database Syst Rev*, 2013(6): CD001877.

    https://doi.org/10.1002/14651858.CD001877.pub5

11. Brem RF, Lenihan MJ, Lieberman J, *et al*., 2015, Screening breast ultrasound: Past, present, and future. *Am J Roentgenol*, 204(2): 234–240.

    https://doi.org/10.2214/AJR.13.12072

12. Hambly NM, Liberman L, Dershaw DD, *et al*., 2011, Background parenchymal enhancement on baseline screening breast MRI: Impact on biopsy rate and short-interval follow-up. *Am J Roentgenol*, 196(1): 218–224.

    https://doi.org/10.2214/AJR.10.4550

13. Mehnati P, Tirtash MJ, 2015, Comparative efficacy of four imaging instruments for breast cancer screening. *Asian Pac J Cancer Prev*, 16(15): 6177–6186.

    https://doi.org/10.7314/apjcp.2015.16.15.6177

14. Gutierrez RM, Cerquera EA, Mañana G, 2012, MPGD for breast cancer prevention: A high resolution and low dose radiation medical imaging. *J Instrum*, 7(7): C07007.

    https://doi.org/10.1088/1748-0221/7/07/C07007

15. Wang L, 2017, Early diagnosis of breast cancer. *Sensors (Basel)*, 17(7): 1572.

    https://doi.org/10.3390/s17071572

16. Breastcancer.org (2006). Your Guide to the Breast Cancer Pathology Report. Available from: https://www.breastcancer.org [Last accessed on 2022 Nov 15].

17. Sahu A, 2012, Hyperspectral Imaging to Discern Malignant and Benign Canine Mammary Tumors a Thesis Proposal Submitted to the Temple University Graduate Board By Amrita Sahu.

18. Ouyang Y, Tsui P, Wu S, *et al*., 2019, Classification of benign and malignant breast tumors using H-scan ultrasound imaging. *Diagnostics (Basel)*, 9(4): 182.

https://doi.org/10.3390/diagnostics9040182

19. Merrill AL, Coopey SB, Tang R, *et al*., 2016, Implications of new lumpectomy margin guidelines for breast-conserving surgery: Changes in reexcision rates and predicted rates of residual tumor. *Ann Surg Oncol*, 23(3): 729–734.

https://doi.org/10.1245/s10434-015-4916-2

20. Vos EL, Jager A, Verhoef C, *et al*., 2015, Overall survival in patients with a re-excision following breast conserving surgery compared to those without in a large population-based cohort. *Eur J Cancer*, 51(3): 282–291.

https://doi.org/10.1016/j.ejca.2014.12.003

21. Kho E, Dashtbozorg B, de Boer LL, *et al*., 2019, Broadband hyperspectral imaging for breast tumor detection using spectral and spatial information. *Biomed Opt Express*, 10(9): 4496.

https://doi.org/10.1364/boe.10.004496

22. Boyce BF, 2017, An update on the validation of whole slide imaging systems following FDA approval of a system for a routine pathology diagnostic service in the United States. *Biotech Histochem*, 92(6): 381–389.

https://doi.org/10.1080/10520295.2017.1355476

23. Evans AJ, Bauer TW, Bui MM, *et al*., 2018, US Food and Drug Administration approval of whole slide imaging for primary diagnosis: A key milestone is reached and new questions are raised. *Arch Pathol Lab Med*, 142(11): 1383–1387.

https://doi.org/10.5858/arpa.2017-0496-CP

24. Flotte TJ, Bell DA, 2018, Anatomical pathology is at a crossroads. *Pathology*, 50(4): 373–374.

https://doi.org/10.1016/j.pathol.2018.01.003

25. Motomura K, Inaji H, Komoike Y, *et al*., 2000, Intraoperative sentinel lymph node examination by imprint cytology and frozen sectioning during breast surgery. *Br J Surg*, 87(5): 597–601.

https://doi/org/10.1046/j.1365-2168.2000.01423.x

26. Flett MM, Going JJ, Stanton PD, *et al*., 1998, Sentinel node localization in patients with breast cancer. *Br J Surg*, 85(7): 991–993.

https://doi.org/10.1046/j.1365-2168.1998.00746.x

27. Van Diest PJ, Torrenga H, Borgstein PJ, *et al*., 1999, Reliability of intraoperative frozen section and imprint cytological investigation of sentinel lymph nodes in breast cancer. *Histopathology*, 35(1): 14–18.

https://doi.org/10.1046/j.1365-2559.1999.00667.x

28. Aref M, Youssef AB, Hussein AA, *et al*., 2022, Custom fluorescence imaging system exploiting hyperspectral camera to characterize and diagnose RNA breast cancer. *Biointerface Res Appl Chem*, 12(4): 5548–5566.

https://doi.org/10.33263/BRIAC124.55485566

29. Welch AJ, Van Gemert MJ, 2011, Optical-Thermal Response of Laser-Irradiated Tissue Vol. 2. Berlin: Springer.

30. Bioucas-Dias JM, Plaza A, Camps-Valls G, *et al*., 2013, Hyperspectral remote sensing data analysis and future challenges. *IEEE Geosci Remote Sens Magazine*, 1(2): 6–36.

31. Adão T, Hruška J, Pádua L, *et al*., 2017, Hyperspectral imaging: A review on UAV-based sensors, data processing and applications for agriculture and forestry. *Remote Sens*, 9(11): 1110.

https://doi.org/10.3390/rs9111110

32. Robles-Kelly A, Huynh CP, 2013, Imaging spectroscopy for scene analysis. In: *Imaging Spectroscopy for Scene Analysis*. Berlin: Springer.

https://doi.org/10.1007/978-1-4471-4652-0

33. Lu G, Fei B, 2014, Medical hyperspectral imaging: A review. *J Biomed Opt*, 19(1): 10901.

https://doi.org/10.1117/1.JBO.19.1.010901

34. Fabelo H, Ortega S, Lazcano R, *et al*., 2018, An intraoperative visualization system using hyperspectral imaging to aid in brain tumor delineation. *Sensors (Basel)*, 18(2): 430.

https://doi.org/10.3390/s18020430

35. Goto A, Nishikawa J, Kiyotoki S, *et al*., 2015, Use of hyperspectral imaging technology to develop a diagnostic support system for gastric cancer. *J Biomed Opt*, 20(1): 16017.

https://doi.org/10.1117/1.JBO.20.1.016017

36. Regeling B, Thies B, Gerstner AO, *et al*., 2016, Hyperspectral imaging using flexible endoscopy for laryngeal cancer detection. *Sensors (Basel)*, 16(8): 1288.

https://doi.org/10.3390/s16081288

37. Aref MH, Youssef AB, Aboughaleb IH, *et al*., 2021, Prospective study for commercial and low-cost hyperspectral imaging systems to evaluate thermal tissue effect on bovine liver samples. *J Spectral Imaging*, 10: a5.

38. Aref MH, Aboughaleb IH, Youssef AB, *et al*., 2021, Hyperspectral image-based analysis of thermal damage for *ex-vivo* bovine liver utilizing radiofrequency ablation. *Surg Oncol*, 38: 101564.

https://doi.org/10.1016/j.suronc.2021.101564

39. El-Sharkawy YH, Aref MH, Elbasuney S, *et al*., 2022, Oxygen saturation measurements using novel diffused reflectance with hyperspectral imaging: Towards facile COVID-19

diagnosis. *Opt Quantum Electron*, 54(5): 322.

https://doi.org/10.1007/s11082-022-03658-z

40. Aref MH, Sharawi AA, El-Sharkawy YH, 2021, Delineation of the arm blood vessels utilizing hyperspectral imaging to assist with phlebotomy for exploiting the cutaneous tissue oxygen concentration. *Photodiagnosis Photodyn Ther*, 33: 102190.

https://doi.org/10.1016/j.pdpdt.2021.102190

41. Aref M, Youssef AB, Hussein AA, *et al*., 2021, Custom fluorescence imaging system exploiting hyperspectral camera to characterize and diagnose RNA breast cancer. *Biointerface Res Appl Chem*, 2: 5548–5566.

42. Aref MH, Abbass MA, Youssef AB, *et al*., 2022, Optical Characterization of Biological Tissues in Visible and Near-Infrared Spectra. In: *2022 13th International Conference on Electrical Engineering (ICEENG)*. IEEE. p. 159–163.

43. Aboughaleb IH, Matboli M, Shawky SM, *et al*., 2021, Transcriptome spectral analysis using hyperspectral imaging for hepatocellular carcinoma detection. *QJM Int J Med*, 114(Suppl 1): hcab088-004.

44. Bashkatov AN, Genina EA, Kochubey VI, *et al*., 2005, Optical properties of human skin, subcutaneous and mucous tissues in the wavelength range from 400 to 2000 nm. *J Phys D Appl Phys*, 38(15): 2543–2555.

https://doi.org/10.1088/0022-3727/38/15/004

45. Ostantini IR, Icchi RI, Ilvestri LU, *et al*., 2019, *In-vivo* and *ex-vivo* optical clearing methods for biological tissues : Review. *Biomed Opt Express*, 10(10): 5251–5267.

https://doi.org/10.1364/BOE.10.005251

46. Tuchin VV, 1997, Light scattering study of tissues. *Phys Uspekhi*, 40(5): 495–515.

https://doi.org/10.1070/pu1997v040n05abeh000236

47. Aref MH, Youssef AB, Aboughaleb IH, *et al*., 2021, Characterization of normal and malignant breast tissues utilizing hyperspectral images and associated differential spectrum algorithm. *J Biomed Photon Eng*, 7(2): 1–12.

https://doi.org/10.18287/JBPE21.07.020302

48. Fajardo C, Solarte E, 2020, Optical properties of a simple model of soft biological tissue. *J Phys Conf Ser*, 1547: 012026.

https://doi.org/10.1088/1742-6596/1547/1/012026

49. Pogue BW, Patterson MS, 2022, Review of tissue simulating phantoms for optical spectroscopy, imaging and dosimetry. *J Biomed Opt*, 11: 041102.

https://doi.org/10.1117/1.2335429

50. Patterson MS, Wilson BC, Wyman DR, 1991, The propagation of optical radiation in Tissue I. Models of radiation transport and their application. Lasers Med Sci, 6: 155–168.

51. Vo-Dinh T, 2014, *Biomedical Photonics Handbook: Biomedical Diagnostics*. United States: CRC Press.

52. DiPerna RJ, Lions PL, 1989, Ordinary differential equations, transport theory and Sobolev spaces. *Invent Math*, 98(3): 511–547.

https://doi.org/10.1007/BF01393835

53. Rinzema K, Murrer LH, Star WM, 1998, Direct experimental verification of light transport theory in an optical phantom. *J Opt Soc Am A*, 15(8): 2078–2088.

54. Yavari N, 2006, Optical spectroscopy for tissue diagnostics and treatment control. *Transport*, 760: 141–157.

https://doi.org/10.1007/978-1-61779-176-5

55. Xie D, Guo W, 2020, Measurement and calculation methods on absorption and scattering properties of turbid food in Vis/NIR range. *Food Bioprocess Technol*, 13(2): 229–244.

https://doi.org/10.1007/s11947-020-02402-3

56. Noor SS, Michael K, Marshall S, *et al*., 2017, Hyperspectral image enhancement and mixture deep-learning classification of corneal epithelium injuries. *Sensors*, 17(11): 2644.

https://doi.org/10.3390/s17112644

57. Palmer GM, Ramanujam N, 2006, Monte Carlo-based inverse model for calculating tissue optical properties. Part I: Theory and validation on synthetic phantoms. *Appl Opt*, 45(5): 1062–1071.

58. Alexandrakis G, Farrell TJ, Patterson MS, 1998, Accuracy of the diffusion approximation in determining the optical properties of a two-layer turbid medium. *Appl Opt*, 37(31): 7401–7409.

https://doi.org/10.1364/ao.37.007401

59. Prahl SA, van Gemert MJ, Welch AJ, 1993, Determining the optical properties of turbid media by using the adding-doubling method. *Appl Opt*, 32(4): 559–568.

60. Wan S, Anderson RR, Parrish JA, 1981, Analytical modeling for the optical properties of the skin with *in vitro* and *in vivo* applications. *Photochem Photobiol*, 34(4): 493–499.

61. Hourdakis CJ, Perris A, 1995, A monte carlo estimation of tissue optical properties for use in laser dosimetry. *Phys Med Biol*, 40(3): 351–364.

https://doi.org/10.1088/0031-9155/40/3/002

62. Jacques SL, Wang L, 1995, Monte Carlo modeling of light transport in tissues. In: *Optical-Thermal Response of Laser-Irradiated Tissue*. Berlin: Springer. p. 73–100.

63. Peng L, Chen W, Zhou W, *et al*., 2016, An immune-inspired semi-supervised algorithm for breast cancer diagnosis. *Comput Methods Programs Biomed*, 134: 259–265.

https://doi.org/10.1016/j.cmpb.2016.07.020

64. Hossain S, Mohammadi FA, 2016, Tumor parameter estimation considering the body geometry by thermography. *Comput Biol Med*, 76: 80–93.

https://doi.org/10.1016/j.compbiomed.2016.06.023

65. Hossain S, Mohammadi FA, Nejad ET, 2011, Neural network approach for the determination of heat source parameters from surface temperature image. In: *2011 24th Canadian Conference on Electrical and Computer Engineering (CCECE)*. IEEE. p. 1109–1112.

66. Pradipta AR, Tanei T, Morimoto K, *et al*., 2020, Emerging technologies for real-time intraoperative margin assessment in future breast-conserving surgery. *Adv Sci (Weinh)*, 7(9): 1901519.

https://doi/org/10.1002/advs.201901519

67. Halicek M, Fabelo H, Ortega S, *et al*., 2019, *In-vivo* and *ex-vivo* tissue analysis through hyperspectral imaging techniques: Revealing the invisible features of cancer. *Cancers*, 11(6): 756.

https://doi.org/10.3390/cancers11060756

68. McCormack DR, Walsh AJ, Sit W, *et al*., 2014, *In vivo* hyperspectral imaging of microvessel response to trastuzumab treatment in breast cancer xenografts. *Biomed Opt Express*, 5(7): 2247–2261.

https://doi.org/10.1364/BOE.5.002247

69. Kim B, Kehtarnavaz N, LeBoulluec P, Liu H, *et al*., 2013, Automation of ROI Extraction in Hyperspectral Breast Images. In: *2013 35th Annual International Conference of the IEEE Engineering in Medicine and Biology Society (EMBC)*. IEEE. p. 3658–3661.

70. Pourreza-Shahri R, Saki F, Kehtarnavaz N, Leboulluec P, *et al*., 2013, Classification of *ex-vivo* Breast Cancer Positive Margins Measured by Hyperspectral Imaging. In: *2013 IEEE International Conference on Image Processing, ICIP 2013-Proceedings*. p. 1408–1412.

https://doi.org/10.1109/ICIP.2013.6738289

71. Sterenborg HJ, Kho E, de Boer LL, *et al*., 2014, Hyperspectral imaging for intraoperative margin assessment during breast cancer surgery. *Opt InfoBase Conf Papers*, 2016: 6–9.

https://doi.org/10.1364/ACPC.2016.AF1K.6

72. Bakhshandeh M, Tutuncuoglu SO, Fischer G, *et al*., 2007, Use of imprint cytology for assessment of surgical margins in lumpectomy specimens of breast cancer patients. *Diagn Cytopathol*, 35(10): 656–659.

73. Coudray N, Ocampo PS, Sakellaropoulos T, *et al*., 2018, Classification and mutation prediction from non–small cell lung cancer histopathology images using deep learning. *Nat Med*, 24(10): 1559–1567.

74. Kim SH, Cornacchi SD, Heller B, *et al*., 2013, An evaluation of intraoperative digital specimen mammography versus conventional specimen radiography for the excision of nonpalpable breast lesions. *Am J Surg*, 205(6): 703–710.

https://doi/org/10.1016/j.amjsurg.2012.08.010

75. Ha R, Friedlander LC, Hibshoosh H, *et al*., 2018, Optical coherence tomography: A novel imaging method for post-lumpectomy breast margin assessment-a multi-reader study. *Acad Radiol*, 25(3): 279–287.

https://doi.org/10.1016/j.acra.2017.09.018

76. Wong TT, Zhang R, Hai P, *et al*., 2017, Fast label-free multilayered histology-like imaging of human breast cancer by photoacoustic microscopy. *Sci Adv*, 3(5): e1602168.

https://doi.org/10.1126/sciadv.1602168

77. Moschetta M, Telegrafo M, Introna T, *et al*., 2015, Role of specimen US for predicting resection margin status in breast conserving therapy. *G Chir*, 36(5): 201–204.

https://doi.org/10.11138/gchir/2015.36.5.201

78. Tang R, Saksena M, Coopey SB, *et al*., 2016, Intraoperative micro-computed tomography (micro-CT): A novel method for determination of primary tumour dimensions in breast cancer specimens. *Br J Radiol*, 89(1058): 20150581.

79. Schnabel F, Boolbol SK, Gittleman M, *et al*., 2014, A randomized prospective study of lumpectomy margin assessment with use of MarginProbe in patients with nonpalpable breast malignancies. *Ann Surg Oncol*, 21(5): 1589–1595.

https://doi.org/10.1245/s10434-014-3602-0

80. Dixon JM, Renshaw L, Young O, *et al*., 2016, Intra-operative assessment of excised breast tumour margins using ClearEdge imaging device. *Eur J Surg Oncol*, 42(12): 1834–1840.

https://doi.org/10.1016/j.ejso.2016.07.141

81. Ortega S, Halicek M, Fabelo H, *et al*., 2020, Hyperspectral imaging and deep learning for the detection of breast cancer cells in digitized histological images. *Proc SPIE Int Soc Opt Eng*, 11320: 206–214.